processes

MDPI

Article

Experimental and Numerical Study of Electrospray Pyrolysis Process for Continuous Production of TiO_2 Particles

Ran Wei [1], Jian Wang [1], Wangliang Li [2], Jichuan Wu [3,*] and Weicheng Yan [1,*]

[1] School of Chemistry and Chemical Engineering, Jiangsu University, Zhenjiang 212013, China
[2] Institute of Process Engineering, Chinese Academy of Sciences, Beijing 100000, China
[3] Institute of Fluid Physics, China Academy of Engineering Physics, Mianyang 621000, China
* Correspondence: wujichuan_wjc@foxmail.com (J.W.); yanwc@ujs.edu.cn (W.Y.)

Abstract: In this study, an integrated electrospray pyrolysis process was designed to continuously produce a representative nano-catalyst TiO_2. A numerical model was also developed to simulate the flow behaviors and droplet transport inside the reactor. The electric field model and particle tracking model were coupled to describe the electrospray pyrolysis process. The effects of key parameters, including electrode configurations, applied voltage, droplet charge density, and flow type of carrying gas on the electric field distribution, particle distribution, and particle collection efficiency, were investigated to help the design and optimization of the integrated electrospray pyrolysis reactor. The results show that the electric potential and electric field strength decrease rapidly with increasing distance away from the nozzle. In addition, the results show that the droplet charge is an important parameter affecting the collection efficiency. The investigation of the key parameters shows that applying a voltage on the ring and using the "gas-bleed" introduction method are more conducive to the improvement in the collection efficiency.

Keywords: electrospray; pyrolysis; TiO_2 particles; one-step preparation; particle tracking simulation

Citation: Wei, R.; Wang, J.; Li, W.; Wu, J.; Yan, W. Experimental and Numerical Study of Electrospray Pyrolysis Process for Continuous Production of TiO_2 Particles. *Processes* **2023**, *11*, 291. https://doi.org/10.3390/pr11010291

Academic Editor: Alberto Di Renzo

Received: 2 January 2023
Revised: 11 January 2023
Accepted: 12 January 2023
Published: 16 January 2023

1. Introduction

TiO_2 photocatalysts are widely used in various applications in the environmental and energy fields, including air and water purification, hydrogen evolution, photoelectrochemical conversion, etc. [1–5]. To achieve continuous production of photocatalysts, ultrasonic spraying pyrolysis was mainly used [6–8]. This method employs ultrasound to atomize the precursor solution into droplets and continuously transports them into a high-temperature region for pyrolysis to obtain the final photocatalysts [9]. However, this continuous-preparation method is not suitable for the system with a polymer as the matrix in the precursor solution due to the high viscosity. Electrohydrodynamic atomization (EHDA) is considered to be an efficient and promising preparation method of micro-/nano-materials due to the advantages of a simple device, one-step processing, and a controllable process [10–16]. In the EHDA process, a strong electric field is formed between the grounded substrate and the nozzle [17,18]. When the electric field force overcomes the surface tension of the liquid, the liquid breaks up into small charged droplets. Electrospray pyrolysis is a preparation method combining EHDA technology with droplet flying heat treatment (pyrolysis reactor), which can deal well with the high viscous precursor systems with the assistance of an electric field.

In recent years, many thin film materials have been prepared by electrospray pyrolysis, such as CaP, CdS, CeO_2, $LiCoO_2$, MgO, ZnO, etc. [19]. In addition to the preparation of nano-film materials, many micro/nanoparticles have also been produced by this method. Lenggoro et al. [20] produced non-agglomerated spherical ZnS nanoparticles with a diameter of 20–40 nm by electrospray pyrolysis. Subsequently, a simple colloidal particle classification technology was developed by combining EHDA with aerosol methods [21].

Terada et al. [22] prepared and characterized TiO_2 by electrospray pyrolysis and also explored its photocatalytic hydrogen evolution activity. In the previous research regarding the preparation of nanoparticles by electrospray pyrolysis, most of the works mainly focused on the evaluation of particle size distribution, crystal structure, properties, and functionalities. There is still a lack of detailed information on the electrospray pyrolysis process during the production of micro/nanoparticles.

Numerical simulations of the EHDA process have been carried out for a long time, which provide a theoretical basis for further exploring the preparation process of electrospray pyrolysis [23–27]. Gañán-Calvo et al. [23] developed a numerical model to describe EHDA droplet transport. Wilhelm et al. [24] studied the transport, evaporation, and deposition of a single droplet on the heating substrate by particle tracking for the EHDA system. Rezvanpour et al. [25] developed a computational model to simulate the fluid and particle dynamics in a chambered EHDA process, which was used to predict the drug particle collection efficiency. However, studies on the internal details, droplet transport, and collection efficiency were seldom reported for the electrospray pyrolysis process. These aspects are the key issues that must be considered for the reactor design, process optimization, and large-scale production towards the industrial application of the electrospray pyrolysis technology.

In this study, an integrated electrospray pyrolysis process was developed to continuously produce a representative nano-catalyst TiO_2. A numerical model was also developed to simulate the flow behaviors and droplet/particle transport inside the reactor. The electric field model and particle tracking model were coupled to describe the electrospray pyrolysis process. The effect of key parameters, including applied voltage, electrode configurations, droplet charge density, and flow type of carrying gas on the electric field distribution, particle residence time, and particle collection efficiency, were investigated to help the design and optimization of the integrated electrospray pyrolysis reactor.

2. Experiment Section

2.1. Materials

Tetra-n-butyl titanate, ethanol, polyvinyl pyrrolidone (PVP), and glacial acetic acid are all analytically pure and purchased from Sinopharm Group Co., Ltd., Shanghai, China.

2.2. Experimental Procedure

2.2.1. Conventional Electrohydrodynamic Process

As shown in Figure 1A, the EHDA experimental device consists of a high-voltage power supply (ES20, GAMMA), a syringe (10 mL), a syringe pump (LSP01-1A, Baoding Dichuang Electronic Technology Co., Ltd., Baoding, China), a nozzle (0.5 mm × 60 mm), and collecting device. The syringe with precursor solution controls the flow rate through the injection pump. When the solution passes through the nozzle connected to the positive electrode of the high-voltage power supply, it is atomized, and there is a collection device at the bottom of the nozzle for collection. Unless specially stated, the flow rate of the solution used in the experiment was 1 mL/h. The specific experimental procedures are as follows: (1) an amount of 0.45 g of PVP was dissolved in a mixed solution of 3 mL of tetra-n-butyl titanate, 5 mL of ethanol, and 2 mL of acetic acid to prepare the precursor solution of TiO_2; (2) the syringe with TiO_2 precursor solution is fixed on the syringe pump; (3) put an aluminum foil on the collection device for grounding; and (4) after setting the parameters of the syringe pump, turn on the high voltage power supply to atomize the solution onto the aluminum foil.

2.2.2. Electrospray Pyrolysis Process

The integrated electrospray pyrolysis experimental setup includes the EHDA device and a heating device (tube resistance furnace (SK2)), as shown in Figure 1B. Specifically, a syringe pump is used to control the flow rate of the syringe containing the TiO_2 precursor solution. The solution is atomized when it passes through a nozzle connected to the positive

electrode of a high-voltage power supply. The atomized droplets fall into the pyrolysis reactor. The nitrogen gas fed into the reactor inlet carries the atomized liquid droplets through the high-temperature heating zone. Subsequently, the droplets are solidified to form particles, which are finally collected at the outlet of the reactor with a grounded mesh electrode. The specific experimental steps are as follows: (1) prepare the TiO_2 precursor solution (same as EHDA process), and fix the syringe containing the precursor solution on the syringe pump; (2) ground the collection substrate at the outlet and introduce nitrogen into the reactor from the inlet of the reactor; (3) setup the metal ring; and (4) after setting the parameters of the syringe pump, turn on the high-voltage power supply to atomize the solution. In addition, the distance between the nozzle and the metal ring is 4 cm, and the metal ring is grounded or connected to a low voltage to form a stable electric field between the ring and the nozzle. By controlling the voltage, the precursor solution can be kept in the cone jet mode for continuous atomization of droplets.

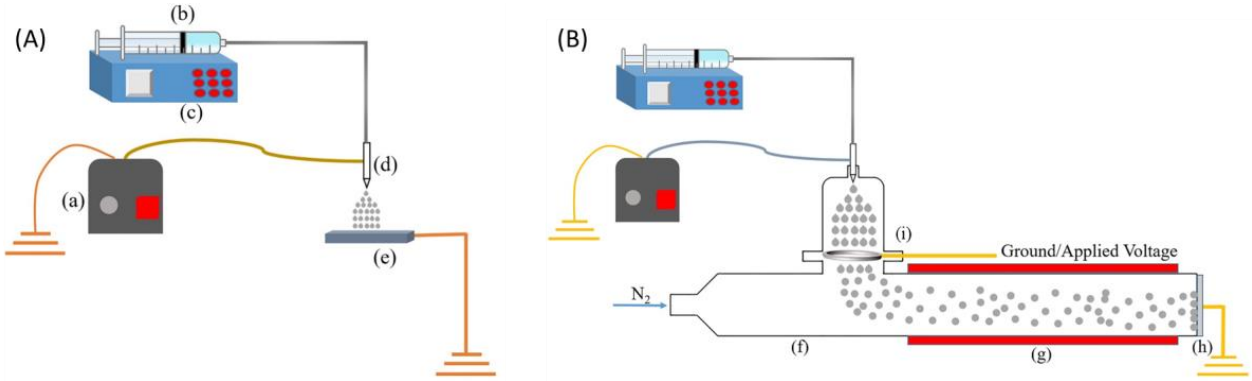

Figure 1. (**A**) Conventional electrohydrodynamic atomization setup; (**B**) electrospray pyrolysis setup. (a) High-voltage power supply; (b) syringe; (c) syringe pump; (d) nozzle; (e) aluminum foil collection substrate; (f) pyrolysis reactor; (g) heating device; (h) aluminum foil with holes; (i) ring electrode.

3. Numerical Simulation

3.1. Governing Equations

A two-phase flow model is chosen for this process, where one phase is the discrete phase (droplet phase), and the other is the continuous phase (nitrogen gas). The mass conservation and momentum conservation equations of the continuous phase can be expressed as [7,8,28]:

$$\nabla \cdot u_f = 0 \tag{1}$$

$$\rho_f \frac{\partial u_f}{\partial t} + \rho_f u_f \cdot \nabla u_f = -\nabla P - \nabla \cdot (\tau) + \rho_f g \tag{2}$$

$$\tau = \mu_f \left[\nabla u_f + (\nabla u_f)^T - \frac{2}{3} \delta \nabla u_f \right]. \tag{3}$$

where ρ_f is the continuous phase density, u_f is the continuous phase velocity, P is the atmospheric pressure, τ is the viscous stress tensor, g is the acceleration due to gravity, u_f is the continuous phase viscosity, and δ is the Kronecker sign function.

The potential distribution can be obtained by solving the Laplace equation:

$$\nabla^2 \phi = 0 \tag{4}$$

The electric field strength distribution can be obtained by solving the Poisson equation:

$$\mathbf{E} = -\nabla \phi \tag{5}$$

where ϕ is the potential and E is the electric field strength.

After the discrete phase (droplet) is ejected from the nozzle, the motion of the droplet (charged particle) is governed by Newton's second law. The force balance for the charged particles is given by:

$$m_p \frac{d\mathbf{u_p}}{dt} = \sum \mathbf{F} = \mathbf{F_D} + \mathbf{F_B} + \mathbf{F_g} + \mathbf{F_E} + \mathbf{F_q} \quad (6)$$

where m_p is the mass of the droplet, $\mathbf{u_p}$ is the velocity of the droplet, $\mathbf{F_D}$ is the drag force, $\mathbf{F_B}$ is the buoyancy force, $\mathbf{F_g}$ is the gravity, $\mathbf{F_E}$ is the electric field force on the droplet, and $\mathbf{F_q}$ is the Coulomb force among the droplets.

$$\mathbf{F_D} = \frac{1}{2} C_D \left(\pi R_p^2\right) \rho_f u_p^2 \quad (7)$$

where R_p is the droplet radius and C_D is the drag force coefficient.

$$C_D = \frac{24}{Re_p}\left(1 + 0.15 Re_p^{0.687}\right) \quad (8)$$

where Re_p is the droplet Reynolds number.

The buoyancy force and gravity can be expressed by [28]

$$\mathbf{F_g} + \mathbf{F_B} = \frac{4}{3}\pi R_p^3 \left(\rho_p - \rho_f\right)\mathbf{g} \quad (9)$$

where ρ_p is the density of droplet.

The electric field force can be calculated by the following formula:

$$\mathbf{F_E} = q\mathbf{E} = -q\nabla\phi \quad (10)$$

where q is the charge carried by the droplet.

The Coulomb repulsion can be calculated by

$$\mathbf{F_q} = \sum_{j=1}^{N} \frac{q \cdot q_j}{4\pi\epsilon_0} \frac{1}{r_j^2} \quad (11)$$

where r_j is the distance between the droplet and other droplet j, and ϵ_0 is the vacuum permittivity.

The collection efficiency at the outlet can be calculated by

$$C_E = \frac{\text{particle number of outlet}}{\text{total}} \times 100\% \quad (12)$$

where "particle number of outlet" represents the number of particles collected at the outlet, and "total" represents the total number of particles.

Information about the radius (R_p) and charge (q) of each droplet can be calculated by the following formula [29,30]:

$$R_p = 1.89\pi^{-\frac{2}{3}} \cdot Q^{\frac{1}{2}} \cdot \left(\frac{\rho_p \epsilon_0}{\gamma K}\right)^{\frac{1}{6}} \cdot f_b \quad (13)$$

$$q_R = 8\pi\epsilon^{\frac{1}{2}}\gamma^{\frac{1}{2}}R_p^{\frac{3}{2}} \quad (14)$$

$$q_{ave} = \frac{4\pi}{3} \cdot R_p^3 \cdot \frac{(\gamma Q K)^{\frac{1}{2}}}{Q} \quad (15)$$

where Q is the liquid flow rate, γ is the surface tension of the liquid, K is the conductivity of the liquid, f_b is the dimensionless radius of the jet at the breaking point ($f_b \approx 0.6$), q_R is

the limit charge carried by the droplet, ϵ is the relative dielectric constant of the liquid, and q_{ave} is the average charge carried by the droplet.

3.2. Geometry and Mesh

According to the dimension of the experimental setup, the geometry and mesh of the computational domain were generated using the COMSOL software. Figure 2a gives the details of the computational domain used to simulate the electrospray pyrolysis process. The nozzle length is 0.01 m, the inner diameter is 2.6×10^{-4} m, and the outer diameter is 5×10^{-4} m. The distance between the nozzle tip and the metal ring was kept at 0.04 m, and the diameters of the thin and thick tubes of the pyrolysis reactor were 0.01 m and 0.03 m, respectively, which was consistent with the experiment. The mesh was built by using the self-adaptive grid function in the COMSOL software, as shown in Figure 2b.

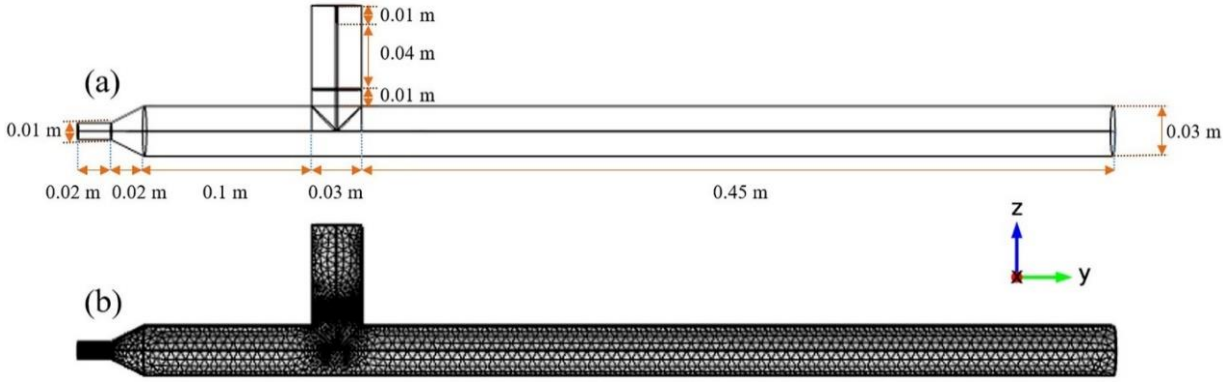

Figure 2. Computational domain of the electrospray pyrolysis reactor: (**a**) physical dimensions; (**b**) mesh.

3.3. Modeling Strategy and Conditions

The electrospray pyrolysis process was simulated by coupling the electric field model with the particle tracking model. First, by solving Equations (4) and (5), an electric field is obtained in the computational domain (Figure 2a). After determining the electric field strength, the flow field information is obtained by solving Equations (1)–(3). According to the flow field information, multiple forces, such as the electric field force, can be determined, and the particle position and velocity can be obtained according to Equations (6)–(11). In addition, the radius (R_p) and charge (q) of each droplet can be calculated by Equations (13)–(15). The model parameters and boundary conditions used in the simulation are shown in Tables 1 and 2.

Table 1. Physical parameters used in simulation.

Parameters	Value
Density of gas (kg/m^3)	1.25
Density of precursor solution (kg/m^3)	948
Viscosity of gas (Pa•s)	1.732×10^{-5}
Conductivity of precursor solution (S/m)	1.2×10^{-5}
Vacuum dielectric constant (F/m)	8.85×10^{-12}
Relative permittivity of the precursor solution	24.5
Relative permittivity of gas	1.00
Surface tension of precursor solution (N/m)	0.022
Solution flow rate (mL/h)	1
Nozzle voltage (V)	6000–9000
Ring voltage (V)	500
Distance from nozzle to ring (m)	0.04
Droplet charge (C)	1.84×10^{-13}
Particle release time step at the inlet (s)	1×10^{-4}
Average droplet size (m)	9.92×10^{-6}

Table 2. Boundary conditions.

Description	Types
Reactor wall	Wall; $\nabla\phi = 0$
Nozzle	Wall; $\phi = \phi_{nozzle}$
Inlet	Velocity inlet; $u = Q/A$
Collection substrate	Adhere; Grounded
The number of droplets released at the entrance	One per release time step
Metal ring	Grounded or 500 V

4. Results and Discussion

4.1. Experimental Results

Figure 3 shows the SEM image of the TiO_2 particles prepared under different operating conditions by both the conventional EHDA process and the integrated electrospray pyrolysis process. Figure 3a,b show the morphology of precursor particles obtained by conventional EHDA. It can be seen that the precursor particles have a smooth surface. Figure 3c,d show the morphology of TiO_2 particles obtained after heating the precursor particles at 500 °C for 20 min. It can be clearly seen that there are wrinkles on the surface of the particles. This may be because the organic components in the precursor particles are pyrolyzed and gasified during the calcination process. In this study, TiO_2 particles were also successfully prepared by using the self-made integrated electrospray pyrolysis device in one step. Figure 3e–h show the morphology images of TiO_2 prepared by electrospray pyrolysis process with ring grounded and ring voltage of 500 V. As shown in Figure 3, the final TiO_2 particle size is much smaller (nanoscale) when using the electrospray pyrolysis method. The experimental results demonstrated the feasibility of this one-step preparation method of TiO_2 nanoparticles by the integrated electrospray pyrolysis device. However, it can be also found that the number of collected particles is much lower than that prepared by the conventional two-step method, indicating that this electrospray pyrolysis device needs to be further optimized to achieve a higher collection efficiency.

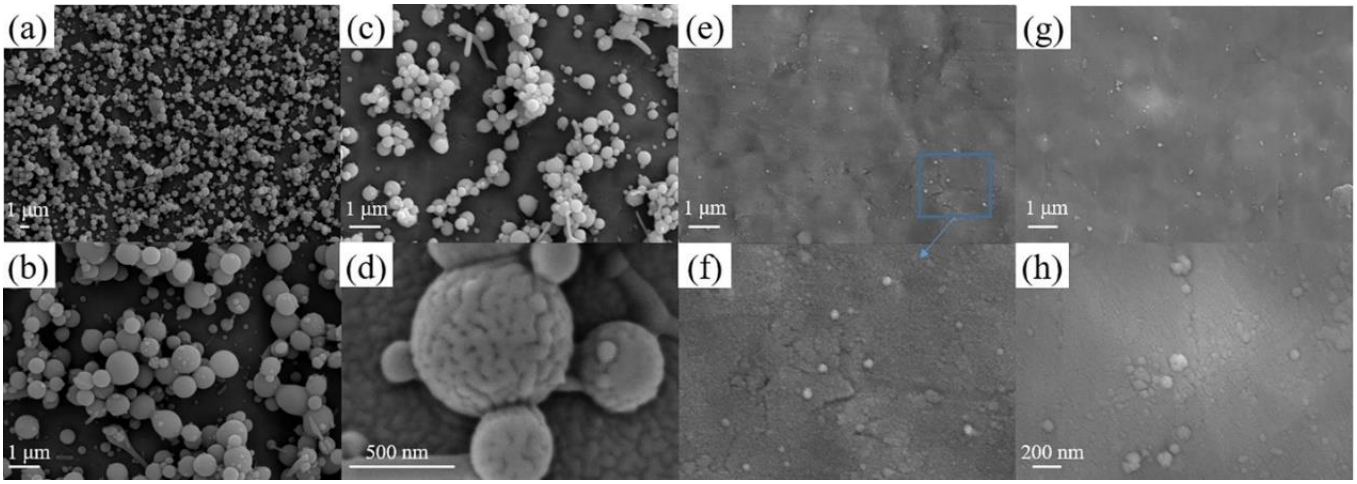

Figure 3. Morphologies of the produced particles under various conditions: (**a**,**b**) precursor particles by conventional EHDA device; (**c**,**d**) TiO_2 particles by calcinating the precursor particles; (**e**,**f**) particles prepared by electrospray pyrolysis with the ring grounded; (**g**,**h**) particles prepared by electrospray pyrolysis with a ring voltage of 500 V.

4.2. Simulation of Electrospray Pyrolysis

To enhance the collection efficiency, a simulation of the electrospray pyrolysis process was carried out to understand the characteristics of the electric field and particle motions inside the reactor. Figure 4 shows the potential distribution under different conditions. It

can be seen that the potential near the nozzle is higher than that in other regions. From the enlarged T-shaped vertical segment, it can be found that the potential drops rapidly along the vertical direction from the nozzle. However, the potential change is not obvious in the T-transverse segment. This is due to the large potential difference between the nozzle and the metal ring. It is worth noting that only by forming a large potential difference can a strong electric field be formed, which is able to atomize the highly viscous liquid. Figure 5 shows the distribution of electric field lines under different applied voltages. Comparing Figure 5a,b, it can be found that the electric field lines only exist in the T-shaped vertical section when grounding the metal ring electrode. This means that if the grounding condition is used for the ring electrode, the droplet is easily deposited on the metal ring under the action of the electric field. It is worth noting that there is an upward folding phenomenon for the electric field lines under both conditions, which may make the droplets stick to the tube wall at the T-junction. Based on the electric field line distributions, a low positive voltage on the metal ring is suggested to avoid the adhesion of particles on the metal ring, which may enhance the particle collection efficiency.

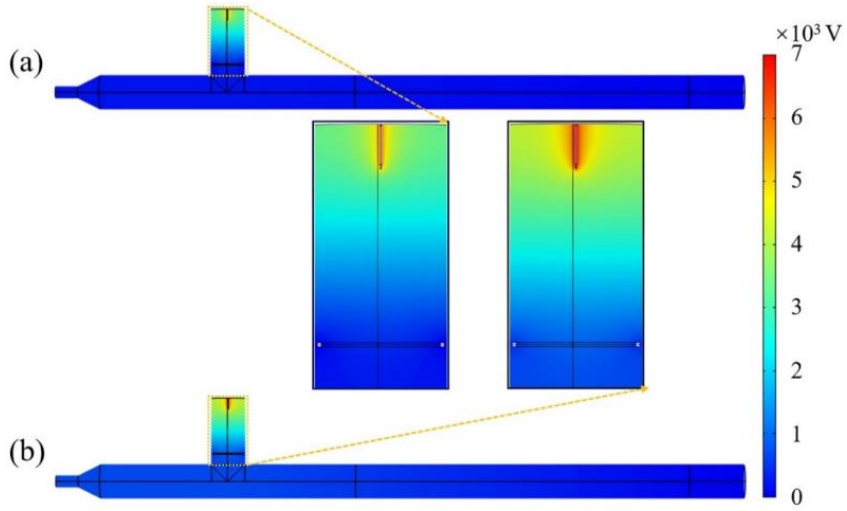

Figure 4. Potential distributions with different applied voltages on the nozzle and ring electrodes: (**a**) nozzle voltage of 6000 V, ring grounded; (**b**) nozzle voltage of 7000 V, ring voltage of 500 V. Operating conditions: N_2 flow rate is 4 L/min, and the droplet charge number is 1.84×10^{-13} C.

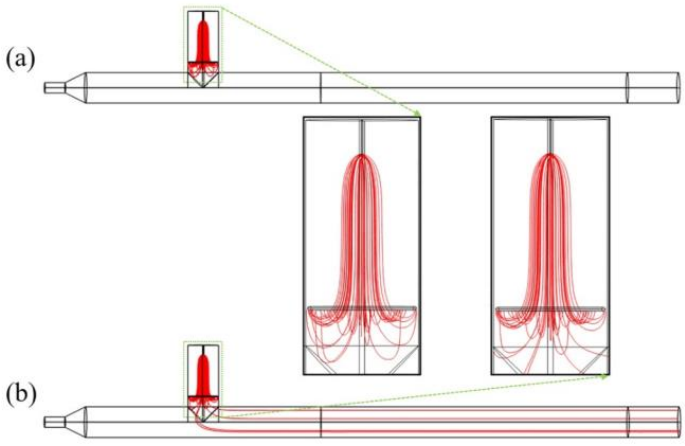

Figure 5. Distribution of electric field lines with different applied voltages on the nozzle and ring electrodes: (**a**) nozzle voltage of 6000 V, ring grounded; (**b**) nozzle voltage of 7000 V, ring voltage of 500 V. Operating conditions: N_2 flow rate is 4 L/min, and the droplet charge number is 1.84×10^{-13} C.

The electric field force on the droplet is the most important force affecting the flow of the droplet during the entire preparation process. The electric field force formula $\mathbf{F_E} = q_E$ indicates that the electric field force on the droplet is related to the charge and electric field strength. The electric field force determines whether the atomized droplets can fall smoothly through the T-vertical section to the pyrolysis section and be successfully driven by the carrying gas nitrogen to the outlet for collection. Therefore, it is necessary to analyze the electric field strength along different directions. The electric field strengths E_z and E_y represent the Z-component and Y-component of the electric field strength, respectively. Figure 6A shows the contour of E_z throughout the entire reactor. It can be seen that the electric field strength at the tip of the nozzle changes drastically, and the electric field strength E_z in other regions is basically the same. This is because the high voltage is applied at the nozzle and the electric potential drops significantly at the region near the tip. The electric field strength E_z along the white line labeled in Figure 6A is shown in Figure 6B. From Figure 6B, it can be found that the electric field strength along the Z direction follows the same trend, although the applied voltage on the nozzle and ring electrode are different. This is because the electric field strength is correlated to the gradient of the electric potential. Although the nozzle voltage and ring voltage are different, the potential difference ($\Delta\phi$) between these two configurations is small (~500V). Since the locations of the electrodes are not changed as well, the trend of the electric field strength will be similar. E_z drops rapidly as the distance from the nozzle increases. Below the nozzle (z = 0.065 m), the electric field intensity E_z with a ring voltage of 500 V is stronger than that with a ring grounded.

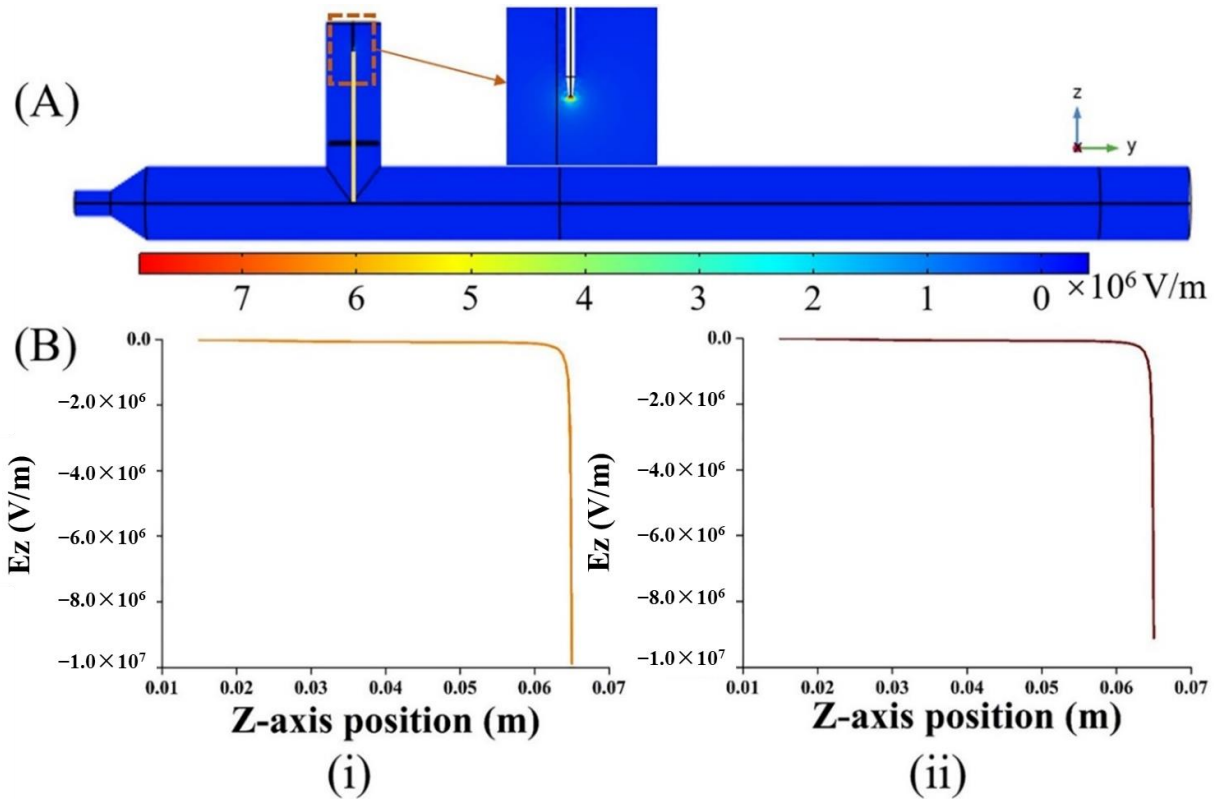

Figure 6. (**A**) Contour of Z-component of electric field strength. (**B**) Distribution of Ez along vertical direction below the nozzle with different applied voltages on the nozzle and ring electrode: (i) nozzle voltage of 6000 V and grounded ring; (ii) nozzle voltage of 7000 V and ring voltage of 500 V.

Figure 7 shows the distribution of the Y-component of the electric field strength, E_y, in the pyrolysis section from the gas inlet to the outlet. Comparing Figure 7a,b, it can be found that the applied voltage on the nozzle and ring electrode has a greater impact on the Y-component of the electric field strength. There is a sudden change in the electric field

intensity at the region near the T-shaped junction. A stronger electric field strength from the T-junction to the outlet can be observed. The electric field strength E_y is 1600 V/m for the case with a ring voltage of 500 V, which is about 1000 V/m higher than that with a grounded ring. The greater E_y is along the *Y*-axis direction, the greater the electric field force is provided, which is conducive to the motion of droplets along this direction. A higher collection efficiency of particles on the outlet may be achieved. In addition, it can be seen that E_y has a negative value for the case with a grounded ring, which means that the direction of the electric field force is opposite to the direction of the *Y*-axis (flow direction). This can lead to disordered droplet flow, which may cause more droplets to stick to the wall.

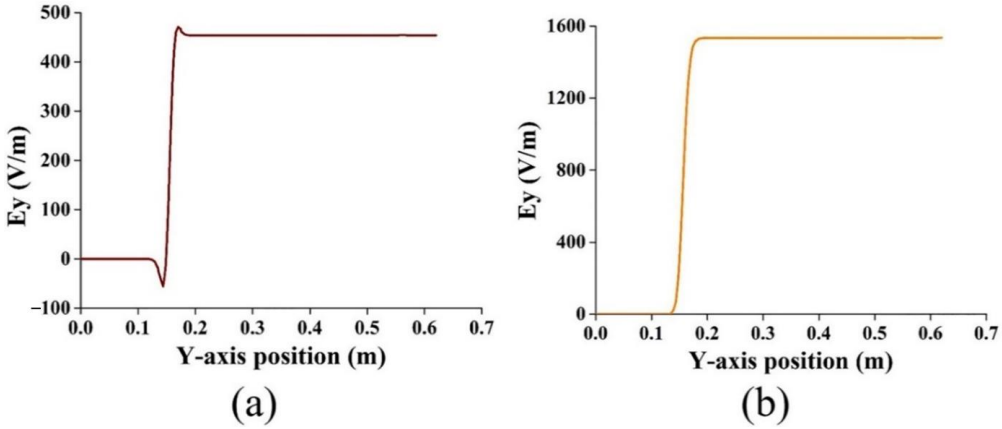

Figure 7. Distribution of Ey along Y direction from the gas inlet to the outlet with different applied voltages on the nozzle and ring electrode: (**a**) nozzle voltage of 6000 V and grounded ring; (**b**) nozzle voltage of 7000 V and ring voltage of 500 V.

Figure 8 shows the particle distribution with different applied voltages on the nozzle and ring electrode. It can be found that most of the droplets gather near the T-junction of the reactor. Compared with the case operated with a grounded ring electrode, the adhesion wall position of the droplet is relatively dispersed for the one with a ring voltage of 500 V. This is also consistent with the above speculation that a voltage applied to the metal ring is more conducive to the flow of droplets due to a stronger electric field between T junction and outlet. Figure 9 shows the collection efficiency, which further confirms the deduction. It can be seen that the collection efficiency for the case with a ring voltage of 500 V is about 67% higher than that with a grounded ring. In summary, it can be concluded that a stronger electric field between the ring and the outlet is conducive to particle collection. However, it is worth noting that the collection efficiency for both cases is still too low; therefore, the designed electrospray pyrolysis process needs further improvement and optimization.

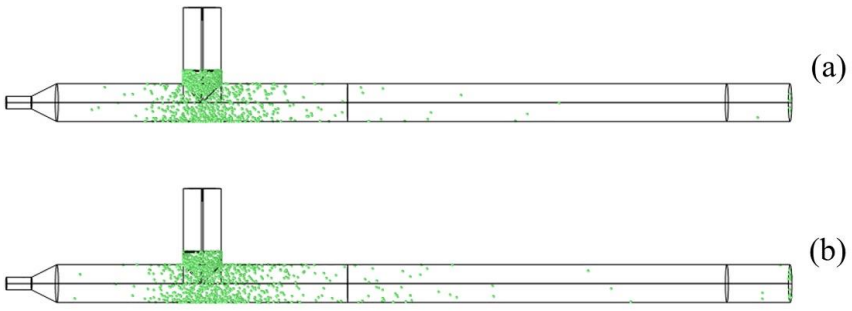

Figure 8. Particle distribution with different applied voltages on the nozzle and ring electrode: (**a**) nozzle voltage of 6000 V and grounded ring; (**b**) nozzle voltage of 7000 V and ring voltage of 500 V.

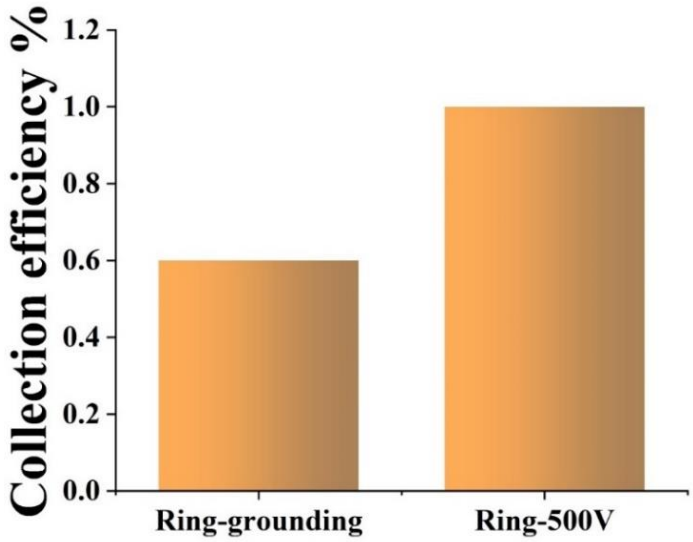

Figure 9. Collection efficiency of particles with different applied voltages on the nozzle and ring electrode.

4.3. Effect of Key Parameters

According to the previous section, the droplet flow in the reactor is mainly affected by the electric field force. The electric field force on the droplet is related to the charge of the droplet and the strength of the electric field. Considering that the droplet charge q will change with the applied voltage, the droplet charge during the preparation process may not be exactly the same as the previously selected value for different operating conditions. Therefore, the influence of the droplet charge on the collection efficiency was further explored. In the process of electrospray, the charged amount of droplets under the steady cone jet can exist in a certain range of values, which is also described in Equations (13)–(15). The selected droplet charge q has a relationship which is $q_{ave} \leq q \leq q_R$. Figure 10 shows the particle collection efficiency for different charge amounts. It can be found that within the range of $q_{ave} \leq q \leq q_R$., the collection efficiency decreases with the increase in the charge amount. This may be because the larger amount of the charge carried by the droplet, the greater the repulsion force received by the surrounding droplets, leading to intensive expansion of the droplets. Therefore, more droplets may adhere to the wall of the vertical section of the reactor. The collection efficiency for the case with the average charge is 27% higher than that with the limit charge. The results indicate that the droplet charge is an important parameter affecting the collection efficiency.

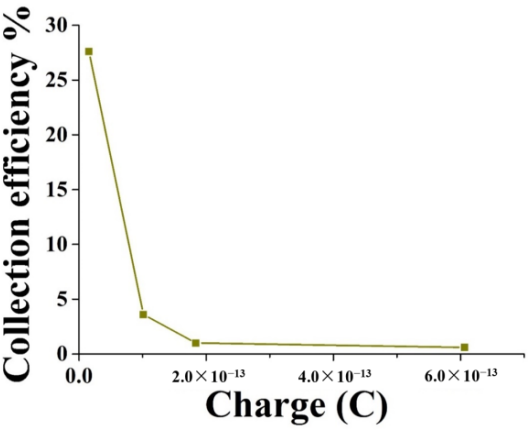

Figure 10. Variations in particle collection efficiency with droplet charge number. Operating conditions: N_2 flow rate is 4 L/min, nozzle voltage is 7000 V, ring voltage is 500 V.

Different experimental operating parameters have different effects on the collection efficiency. Exploring the effect of different operating parameters on the collection efficiency is the key to the subsequent optimization design. Figure 11 shows the variation in particle collection efficiency with different operating parameters. Figure 11a describes the effect of different nitrogen flow rates on the collection efficiency. The results show that the collection efficiency slightly increases with the nitrogen flow rate when the charge is equal to q_R. The reason for this phenomenon is that when the charge amount on the droplet is high enough, the gas drag force is much smaller than the electric field force. The droplet motion is mainly dominated by the electric field; therefore, the flow rate has less impact on the collection efficiency. When the droplet charge is equal to q_{ave}, the collection efficiency increases with the increase in the nitrogen flow rate from 2 L/min to 4 L/min and then decreases as the nitrogen flow rate further increases from 4 L/min to 10 L/min. When the charge of the droplet is small, the driving force of nitrogen gas is the dominant force affecting the flow of the droplet. As the driving force from the carrying gas increases, more particles can be collected at the outlet. However, if the driving force of nitrogen gas is too large, most of the droplets are blown and adhered to the wall when the droplets flow from the nozzle to the T-shaped junction. The number of droplets entering the T-shaped-transverse section pipeline is less, which lowers the final collection efficiency.

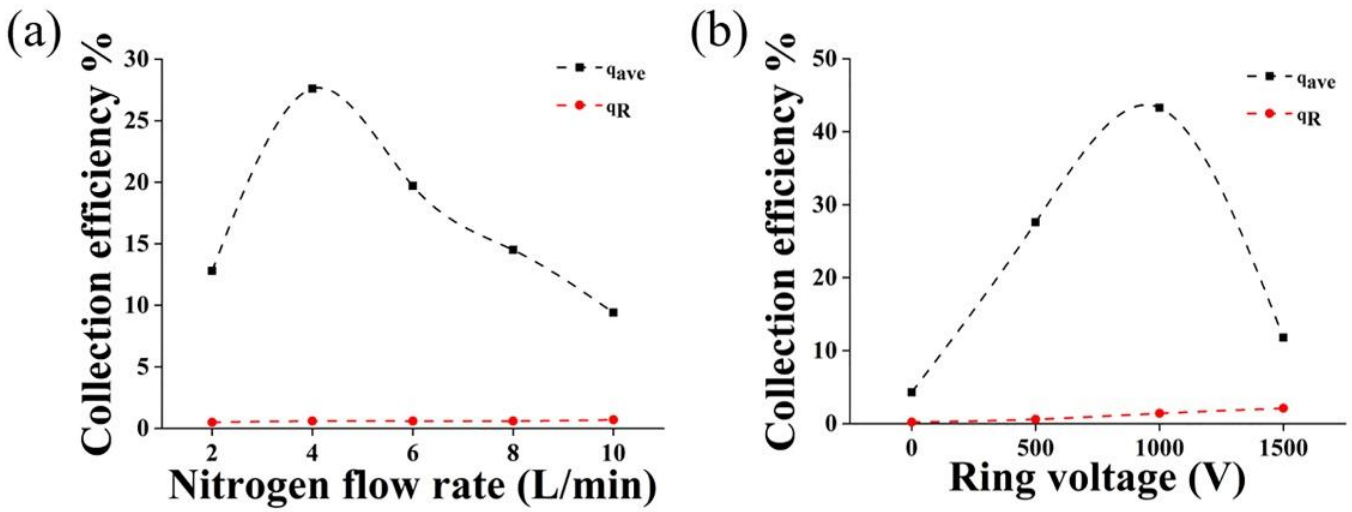

Figure 11. Variations in particle collection efficiency with (**a**) N_2 flow rate (2–10 L/min) and (**b**) ring voltage (0–1500 V).

Figure 11b describes the effect of different ring voltage values on the collection efficiency. The difference between the nozzle voltage and the ring voltage is kept at 6500 V. Similarly, it can be found that the collection efficiency slightly increases with the ring voltage when the charge amount is q_R. Additionally, the collection efficiency is much lower than that with q_{ave} as the charge amount on the droplet. This is because the greater the charge of the droplet, the greater the repelling force the droplet receives. Therefore, the droplets are easy to adhere to the T-shaped-vertical section of the pipe wall, and fewer droplets fall into the T-shaped-horizontal section of the pipeline. When the droplet charge is q_{ave}, the collection efficiency first increases and then decreases with the increase in the ring voltage from 0 to 1500 V. The collection efficiency can reach up to 43.3% when 1000 V is applied to the ring electrode. As the ring voltage increases, the electric field formed between the metal ring and the outlet will increase. The electric field force on the droplet along the *Y*-axis direction increases, thereby reducing the number of wall adhesions and increasing the number of droplets flying to the outlet. However, as the electric field is strengthened, once the downward electric field force of the droplet is equal to or greater

than the driving force of the gas to the outlet, the droplet is more likely to fall on the lower wall of the T-shaped junction. Therefore, the collection efficiency decreases.

To investigate the effect of the introduction method of carrying gas on the collection efficiency, different feeding methods of nitrogen were further discussed based on the operating parameters selected during the experiment. Figure 12 shows the collection efficiencies for the cases with different gas introduction methods. The collection efficiency reaches 38% when the "gas-bleed" mode and a droplet charge equal to q_{ave} are used (Figure 12a). When the droplet charge is equal to 6.06×10^{-13} C, the collection efficiency drops to ~2% (Figure 12b). For both cases, it is obvious that the collection efficiency by "gas-bleed" mode is higher than that by "gas-blow". This suggests that the "gas-bleed" mode may be used to further increase the collection efficiency when the other parameters have been optimized.

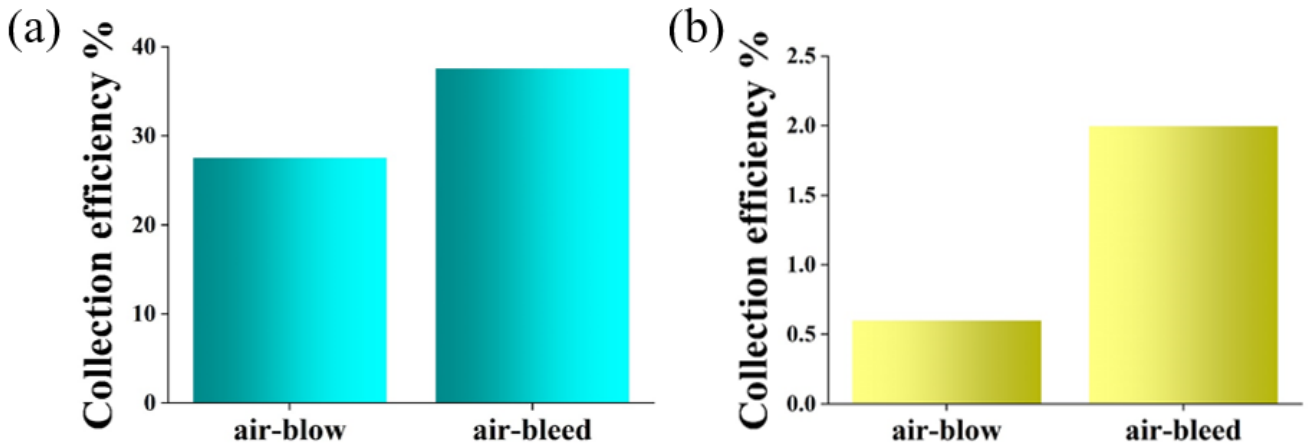

Figure 12. Comparison of collection efficiency with "gas-blow" and "gas-bleed" gas introduction methods: (**a**) droplet charge number $q_{ave} = 1.57 \times 10^{-14}$ C; (**b**) droplet charge number $q_R = 6.06 \times 10^{-13}$ C.

5. Conclusions

In this study, TiO_2 nanoparticles were successfully prepared in one step using a self-made integrated electrospray pyrolysis device, demonstrating the ability of this method to continuously produce nanoparticles in a single step. The electrospray pyrolysis process was simulated by coupling the electric field model with the particle tracking model. Simulation results show that the electric potential and electric field strength decrease rapidly with increasing distance away from the nozzle. In addition, the results also show that the droplet charge is an important parameter affecting the collection efficiency. The optimization and design results based on the electrospray pyrolysis process show that applying a voltage on the ring and using the "gas-bleed" gas introduction method are more conducive to the improvement in the collection efficiency. Therefore, the combination of a ring with voltage and the "gas-bleed" mode is suggested for the continuous preparation of TiO_2 nanoparticles by integrated electrospray pyrolysis.

Author Contributions: Conceptualization, W.Y. and R.W.; methodology, J.W. (Jian Wang) and R.W.; software, R.W. and J.W. (Jian Wang); validation, J.W. (Jian Wang) and J.W. (Jichuan Wu); formal analysis, W.L. and W.Y.; investigation, J.W. (Jian Wang); data curation, J.W. (Jian Wang) and R.W.; writing—original draft preparation, J.W. (Jian Wang), R.W. and W.Y.; writing—review and editing, J.W. (Jichuan Wu); visualization, W.L. and J.W. (Jian Wang); supervision, W.Y.; project administration, W.Y.; funding acquisition, W.Y. All authors have read and agreed to the published version of the manuscript.

Funding: This research was funded by the National Natural Science Foundation of China, grant number 21808088, and the Innovation and Entrepreneurship Program of Jiangsu Province, grant number (2020)10545.

Data Availability Statement: The data that support the findings of this study are available within the article.

Conflicts of Interest: The authors declare no conflict of interest.

References

1. Xiao, X.; Zhu, W.W.; Liu, Q.Y.; Yuan, H.; Li, W.W.; Wu, L.J.; Li, Q.; Yu, H.Q. Impairment of biofilm formation by TiO2 photocatalysis through quorum quenching. *Environ. Sci. Technol.* **2016**, *50*, 11895–11902. [CrossRef] [PubMed]
2. Guo, F.; Sun, H.; Huang, X.; Shi, W.; Yan, C. Fabrication of TiO2/high-crystalline g-C3N4 composite with enhanced visible-light photocatalytic performance for tetracycline degradation. *J. Chem. Technol. Biotechnol.* **2020**, *95*, 2684–2693.
3. Wang, H.; Chu, J.; Ou, H.; Zhao, R.; Han, J. Analysis of TiO2 photocatalysis in a pulsed discharge system for phenol degradation. *J. Electrost.* **2009**, *67*, 886–889. [CrossRef]
4. Liu, X.L.; Guo, W.L.; Ma, J.J. Hydrothermal preparation of B-doped TiO2 and photodegradation of salicylic acid under visible light. *Adv. Mat. Res.* **2012**, *557*, 1592–1595.
5. Nakata, K.; Fujishima, A. TiO2 photocatalysis: Design and applications. *J. Photochem.* **2012**, *13*, 169–189. [CrossRef]
6. Tsai, S.C.; Song, Y.L.; Tsai, C.S.; Yang, C.C.; Chiu, W.Y.; Lin, H.M. Ultrasonic spray pyrolysis for nanoparticles synthesis. *J. Mater. Sci.* **2004**, *39*, 3647–3657. [CrossRef]
7. Wang, J.; Feng, F.; Wang, C.; Yan, W.C.; Shi, W. Experimental and numerical study of the ultrasonic atomization pyrolysis process toward mass production of photocatalysts. *Ind. Eng. Chem. Res.* **2020**, *59*, 11777–11789. [CrossRef]
8. Wang, J.; Wu, J.; Yuan, S.; Yan, W.C. CFD simulation of ultrasonic atomization pyrolysis reactor: The influence of droplet behaviors and solvent evaporation. *Int. J. Chem. React. Eng.* **2021**, *19*, 167–178. [CrossRef]
9. Ardekani, S.R.; Aghdam, A.S.R.; Nazari, M.; Bayat, A.; Yazdani, E.; Saievar-Iranizad, E. A comprehensive review on ultrasonic spray pyrolysis technique: Mechanism, main parameters and applications in condensed matter. *J. Anal. Appl. Pyrolysis* **2019**, *141*, 104631. [CrossRef]
10. Nie, X.B.; Wang, Y.; Ran, X.; Wu, J.C.; Wei, R.; Yan, W.C. Preparation of Nanoparticle-Loaded Microbubbles via an Electrohydrodynamic Atomization Process. *Appl. Sci.* **2022**, *12*, 3621. [CrossRef]
11. Yan, W.C.; Xie, J.; Wang, C.H. Electrical field guided electrospray deposition for production of gradient particle patterns. *ACS Appl. Mater. Interfaces* **2018**, *10*, 18499–18506. [CrossRef] [PubMed]
12. Davoodi, P.; Feng, F.; Xu, Q.; Yan, W.C.; Tong, Y.W.; Srinivasan, M.P.; Kumar, S.V.; Wang, C.H. Coaxial electrohydrodynamic atomization: Microparticles for drug delivery applications. *J. Control. Release* **2015**, *205*, 70–82. [CrossRef] [PubMed]
13. Davoodi, P.; Ng, W.C.; Yan, W.C.; Srinivasan, M.P.; Wang, C.H. Double-walled microparticles-embedded self-cross-linked, injectable, and antibacterial hydrogel for controlled and sustained release of chemotherapeutic agents. *ACS Appl. Mater. Interfaces* **2016**, *8*, 22785–22800. [CrossRef] [PubMed]
14. Yan, W.C.; Davoodi, P.; Tong, Y.W.; Wang, C.H. Computational study of core-shell droplet formation in coaxial electrohydrodynamic atomization process. *AIChE J.* **2016**, *62*, 4259–4276. [CrossRef]
15. Yan, W.C.; Chua, Q.W.; Ong, X.J.; Sharma, V.K.; Tong, Y.W.; Wang, C.H. Fabrication of ultrasound-responsive microbubbles via coaxial electrohydrodynamic atomization for triggered release of tPA. *J. Colloid Interface Sci.* **2017**, *501*, 282–293. [CrossRef]
16. Yan, W.C.; Tong, Y.W.; Wang, C.H. Coaxial electrohydrodynamic atomization toward large scale production of core-shell structured microparticles. *AIChE J.* **2017**, *63*, 5303–5319. [CrossRef]
17. Wang, C.; Wang, Y.; Shi, W.D.; Yan, W.C. Electric field assisted assembly of nanoparticle loaded microspheres toward industrial applications for organic dye removal. *Sep. Purif. Technol.* **2023**, *306*, 122565. [CrossRef]
18. Nie, X.; Zhang, D.; Yan, W. Research progress of functional microbubble materials. *CIESC J.* **2021**, *72*, 3984–3996.
19. Jaworek, A.T.S.A.; Sobczyk, A.T. Electrospraying route to nanotechnology: An overview. *J. Electrost.* **2008**, *66*, 197–219. [CrossRef]
20. Lenggoro, I.W.; Okuyama, K.; de la Mora, J.F.; Tohge, N. Preparation of ZnS nanoparticles by electrospray pyrolysis. *J. Aerosol Sci.* **2000**, *31*, 121–136. [CrossRef]
21. Okuyama, K.; Lenggoro, I.W. Preparation of nanoparticles via spray route. *Chem. Eng. Sci.* **2003**, *58*, 537–547. [CrossRef]
22. Terada, Y.; Suzuki, Y.; Tohno, S. Synthesis and characterization of TiO_2 powders by electrospray pyrolysis method. *Mater. Res. Bull.* **2012**, *47*, 889–895. [CrossRef]
23. Gañán-Calvo, A.M.; Lasheras, J.C.; Dávila, J.; Barrero, A. The electrostatic spray emitted from an electrified conical meniscus. *J. Aerosol Sci.* **1994**, *25*, 1121–1142. [CrossRef]
24. Wilhelm, O.; Mädler, L.; Pratsinis, S.E. Electrospray evaporation and deposition. *J. Aerosol Sci.* **2003**, *34*, 815–836. [CrossRef]
25. Rezvanpour, A.; Lim, E.W.C.; Wang, C.H. Computational and experimental studies of electrohydrodynamic atomization for pharmaceutical particle fabrication. *AIChE J.* **2012**, *58*, 3329–3340. [CrossRef]
26. Wang, J.; Dong, T.; Cheng, Y.; Yan, W.C. Machine Learning Assisted Spraying Pattern Recognition for Electrohydrodynamic Atomization System. *Ind. Eng. Chem. Res.* **2022**, *61*, 8495–8503. [CrossRef]
27. Dong, T.; Wang, J.X.; Wang, Y.; Tang, G.H.; Cheng, Y.; Yan, W.C. Development of Machine Learning Based Droplet Diameter Prediction Model for Electrohydrodynamic Atomization Systems. *Chem. Eng. Sci.* **2022**, *268*, 118398. [CrossRef]
28. Shi, W.D.; Wang, J.; You, S.; Yan, W.C. Numerical simulation of particle focusing dynamics of DNA-laden fluids in a microtube. *Chem. Eng. Sci.* **2019**, *209*, 115213. [CrossRef]

29. Zeleny, J. Instability of electrified liquid surfaces. *Phys. Rev.* **1917**, *10*, 1–6. [CrossRef]
30. Xie, J.; Jiang, J.; Davoodi, P.; Srinivasan, M.P.; Wang, C.H. Electrohydrodynamic atomization: A two-decade effort to produce and process micro-/nanoparticulate materials. *Chem. Eng. Sci.* **2015**, *125*, 32–57. [CrossRef]